JMEPEG (2007) 16:55–62
DOI: 10.1007/s11665-006-9008-9

1059-9495/$19.00

High Temperature Creep Deformation Mechanisms of a Hot Corrosion-Resistant Nickel-based Superalloy

J.S. Huo, J.T. Gou, L.Z. Zhou, X.Z. Qin, and G.S. Li

(Submitted November 17, 2005; in revised form April 9, 2006)

Creep properties of the experimental superalloy were investigated in the temperature range 1073–1223 K and stress range 110–550 MPa. The observations of dislocation structures during different creep conditions reveal that in the high stress region, particle-shearing mechanisms including stacking fault formation and antiphase boundary creation are operative and in the low stress region, the dislocation climb mechanism is dominant. From the plot of minimum creep rate versus applied stress, a very low stress region with exponent $n < 2$, which is related to diffusional creep, is found. Based on the experimental results, a stress–temperature creep deformation mechanism map for the alloy is constructed. On the basis of particle hardening theories and various dislocation-creep theories, the dislocation-creep transitions in terms of internal stress are discussed and calculated threshold stresses of various creep deformation mechanisms indicates that the particle shearing is easier to operate than Orowan looping at high stresses, and general climb is easy to happen at low stresses.

Keywords creep deformation mechanism, TEM microstructure, threshold stress, nickel-based superalloy

1. Introduction

Cast nickel-based superalloys for modern gas turbines are continually being developed to increase thrust, operating efficiency and durability (Ref 1, 2). The experimental superalloy is designed and employed in high performance industrial gas turbines as low-pressure turbine blades. Working in temperature range of 1023–1173 K, the alloy contains 16% Cr (in wt.%) and 11% Co for sufficient hot-corrosion resistance and high temperature oxidation resistance capability. It contains 7.5% solution elements (W, Mo, Nb) and 7.8% precipitation strengthening elements (Al, Ti), which promote its high strength at high temperature. It is doped with B and Zr elements to reinforce grain boundary. Furthermore, the alloy possesses superior stress rupture capability with no expensive elements, and it is a relatively low cost alloy.

Nickel-based superalloys expend almost all their life in creep deformation processes. Thus, it is worth studying the creep deformation mechanisms at various combinations of stress and temperature. In general, the high temperature creep properties are affected mostly by the microstructural aspects such as solution strengthening, grain boundary phases and especially γ' precipitates. Interactions of coherent γ' particles and dislocations are studied in many literatures (Ref 1–10) and various creep deformation mechanisms are proposed. With combination of the different mechanisms of an alloy at various conditions, a deformation mechanism map can be constructed to provide a powerful tool to develop high temperature alloys, to achieve more resistant alloys, and to rationalize the creep behavior of these alloys.

In this study, tensile creep tests and transmission electron microscope (TEM) observations of specimens crept at different conditions are used to construct a deformation mechanism map for the alloy. Moreover, the dislocation-creep transitions in terms of internal stress are researched. The results of detailed calculation of the threshold stresses are in agreement with experimental observations, which is helpful to understand the various deformation mechanisms in the alloy.

2. Material and Experimental Techniques

The chemical composition of the alloy with weight percent is given in Table 1. The alloy was produced in the vacuum furnace and cast into round bars of 16 mm in diameter and 130 mm in length. Then the bars were given a solution heat treatment (4 h at 1443 K) and a two-step aging treatment (4 h at 1323 K and 16 h at 1123 K).

The specimens with gauge section of ϕ 10×100 mm were machined from the heat-treated bars. The constant load tensile creep tests were conducted in air under the stress range from 140 to 520 MPa and at the temperature range from 1073 to 1223 K. The temperature during creep tests was measured using two thermocouples on the gauge length, and the temperature error was controlled within ±2 K. The inductive transducers could detect strain variation as small as 5×10^{-5}. Most of creep tests were run to rupture, whereas some tests were interrupted for TEM observations. To preserve the dislocation microstructures, foils used for TEM observations were taken from the creep specimens that were fast cooled under load.

Metallographic examination was made on the longitudinal specimen of the creep specimens. The samples used for TEM

J. S. Huo, J. T. Gou, L. Z. Zhou, X. Z. Qin and **G. S. Li,** Department of Superalloys, Institute of Metal Research, Chinese Academy of Sciences Shenyang P. R. China. Contact e-mail: jshou@imr.ac.cn.

observations were firstly ground using silicon carbide papers and then conventional jet polished in a solution of 10% perchloric acid, 2% distilled water, and 88% methanol at 253 K with voltage of 45 V. The microstructure of the thin or transverse foils was analyzed by a Philips TEM 420 (Philips electronics Ltd., Netherlands) transmission electron microscope at 120 kV or a TECNAI G220 (FEI Company, USA) transmission electron microscope at 200 kV.

3. Results and Discussion

3.1 Microscopy of Virgin Material

The microstructure of the heat-treated alloy consists of larger cube γ' (with average edge length of 0.2 μm), fine spherical γ' (with average diameter 0.03 μm), γ/γ' eutectics, carbides and some minor phases. Figure 1(a) and (b) show an optical microstructure and a TEM micrograph, respectively, of the alloy after heat treatment. In the alloy, the carbides and minor phases such as boride distribute mainly at grain boundaries and in interdendritic regions. The MC carbides, which are often in blocky form with the largest dimension exceeding 25 μm, are found in the eutectic colonies. The $M_{23}C_6$ carbides, which are often considered to prevent grain boundary sliding (Ref 4, 7), precipitate mainly at grain boundaries. Although the carbides may play an important role in creep fracture, their contribution to strengthening can be negligible since they are thinly scattered and cannot interfere the motion of dislocations efficiently. The total volume fraction of the γ' particles evaluated with CALPHAD method and measured on SEM micrograph is about 52%. In general, the long range ordered structure of γ' phase affects glide of dislocations markedly, so precipitation strengthening by coherent γ' particles is the main factor for strengthening nickel-based superalloys. In addition, the strength of superalloys also depends on other factors such as γ/γ' lattice mismatch, the matrix/particle interface formation energy, elastic coherency strain, anti-phase boundaries (APB) and/or stacking faults production during dislocation shearing, and different elastic module of the matrix and precipitate (Ref 6–13).

3.2 Creep Tests

The typical creep curves for the alloy are illustrated in Fig. 2 and 3. Figure 2 shows the creep curves of the failed and interrupted creep tests conducted at 245 MPa and different temperatures. In the alloy, a tertiary stage is dominant during high temperature deformation (1223 K), whereas the secondary stage appears more and more obvious with decreasing temperature. Lower temperature tests show significant sigmoid transient deformation, which occurs before steady-state creep, including both softening and hardening process. As the temperature increases, the extent of this sigmoidal transient decreases. Figure 3(a) shows the entire creep curves of the tests conducted at 1173 K and four different stresses. The creep curves exhibit a short primary stage under all stresses, and at high stress (350 MPa), the creep curve is dominated by tertiary stage, and as the stress decreases, a long steady state stage is followed by a short tertiary stage. The creep strain dependence of the creep strain rate is plotted in Fig. 3(b), which shows a strain softening response and a long nearly linear relation between creep rate and the accumulated strain. As pointed out by Nabarro and de Villiers (Ref 2), similar curves indicate that the low strains correspond to the largest part of the creep life. Moreover, the slope of the linear section increases with increasing stress. But it is also noticeable that in the last sections of these curves, creep rate increases rapidly with increasing creep strain, which is the character of the tertiary creep stage.

At the applied temperature above 0.5 T_m (melting temperature), dislocation creep appears in most of superalloys. In the experimental alloy, the dislocation creep is the dominant creep deformation mechanism and can be described by a power law expression:

$$\dot{\varepsilon}_s = A\sigma_c^n \exp(-Q_c/RT) \qquad \text{(Eq 1)}$$

where $\dot{\varepsilon}_s$ is the steady state creep rate, A the structure sensitive constant, σ_c the applied stress, n the apparent stress exponent,

Table 1 Chemical composition of the experimental alloy (wt.%)

C	Cr	Co	W	Mo	Al	Ti	Nb	B	Zr	Ni
0.07–0.11	15.5–15.9	10.8–11	5.3–5.6	1.9–2.1	2.7–3.2	4.4–4.6	0.2–0.3	0.02–0.05	0.05	Bal.

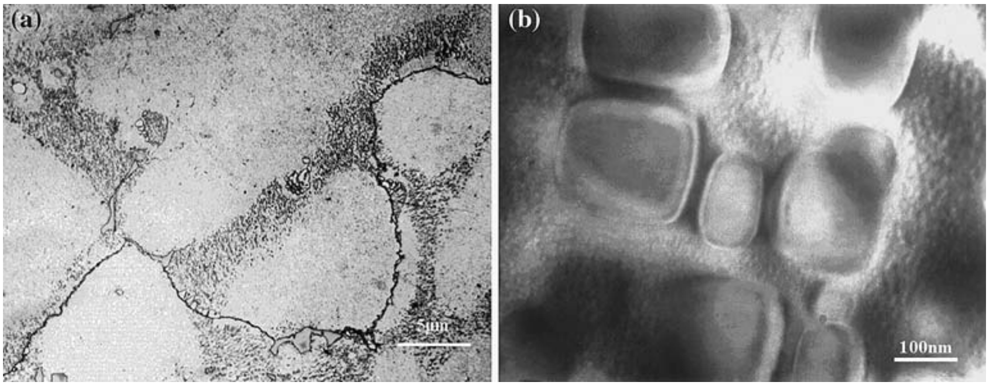

Fig. 1 (a) An optical microstructure and (b) a TEM micrography of the alloy at standard heat treatment state

Q_c the apparent activation energy, R the gas constant, and T the absolute temperature. Equation 1 can be rewritten as $\log\dot{\varepsilon}_s = A' + n\log\sigma$ at constant temperature (A' is a constant), used to determine the values of n. Figure 4 shows the stress and temperature dependence of the steady state creep rate for the alloy at various stresses and in the temperature range of 1073–1223 K. The curve obtained at each temperature consists of two or three straight lines with different slopes. At 1123 and 1173 K, three regions are distinguished. At higher stress regimes and in the temperature range of 1073–1223 K, n = 10.4–12.1, while at the middle stress regimes and in the temperature range of 1123–1223 K, n = 3.8–4.3, and at the lowest stress regimes, the values of n are close to 1. Another form of Eq 1 rewritten as $\ln\dot{\varepsilon}_s = \text{constant} - Q_c/RT$ is used to determine the active energy Q_c. The temperature dependence of the steady-state creep rate of the alloy is plotted in Fig. 5. From limited experimental data, Q_c values of 660 and 285 kJ/mol at different temperature regions are obtained.

The different values of n or different activation energies define different creep mechanisms. For creep diffusion, although early observations reported n = 1 and the creep rate was about 10^{-11} s^{-1} of 1% of total creep strain (Ref 14-16), it was reported recently that the creep rate was often higher than that predicted (Ref 17, 18). Thus, the dominant creep mechanism is diffusional creep in the alloy when the value of n is close to 1 at very low stress levels. In superalloys, the kinetics of diffusional creep is not very clear. Lupinc (Ref 16) pointed out that at lower stress, polycrystals deform due to

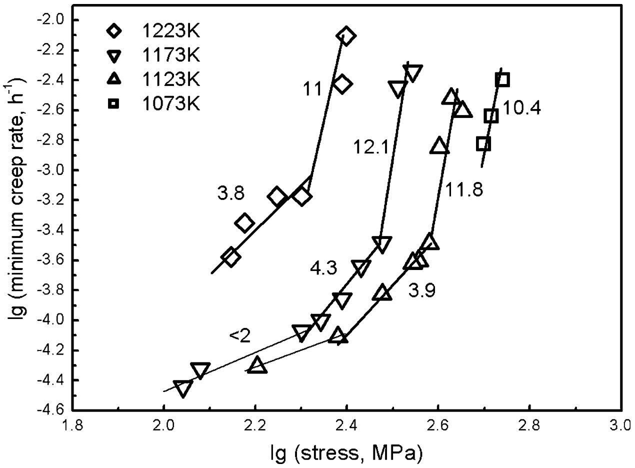

Fig. 4 The stress dependence of the minimum creep rate of the alloy at different temperatures. The values represent apparent stress exponent n for each creep mechanism

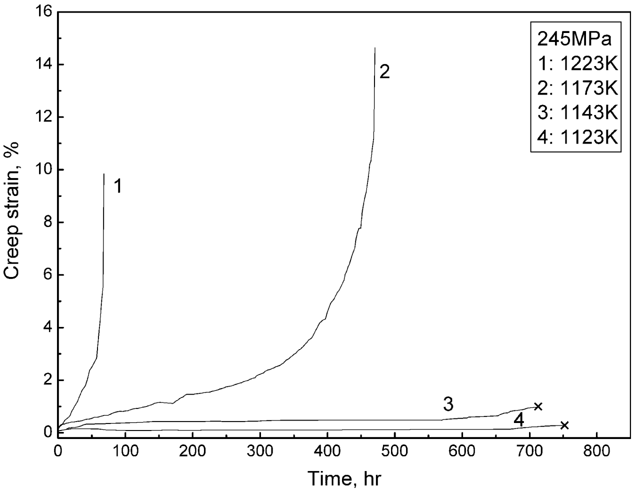

Fig. 2 Experimental creep curves of failed and interrupted tests at 245 MPa and different temperatures

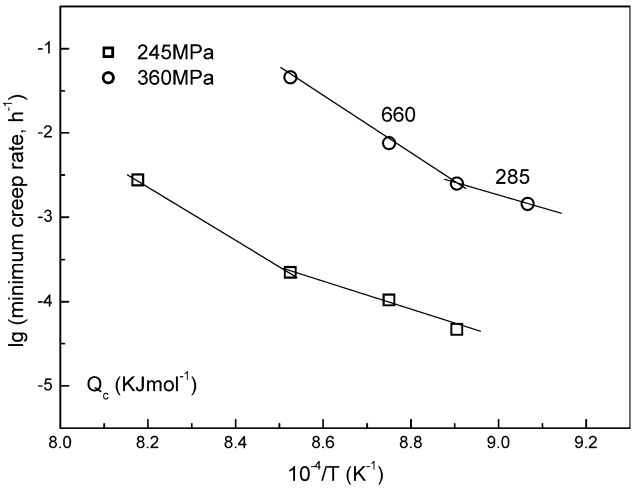

Fig. 5 The temperature dependence of the minimum creep rate at different stresses. The values represent apparent activation energy Q for creep mechanisms

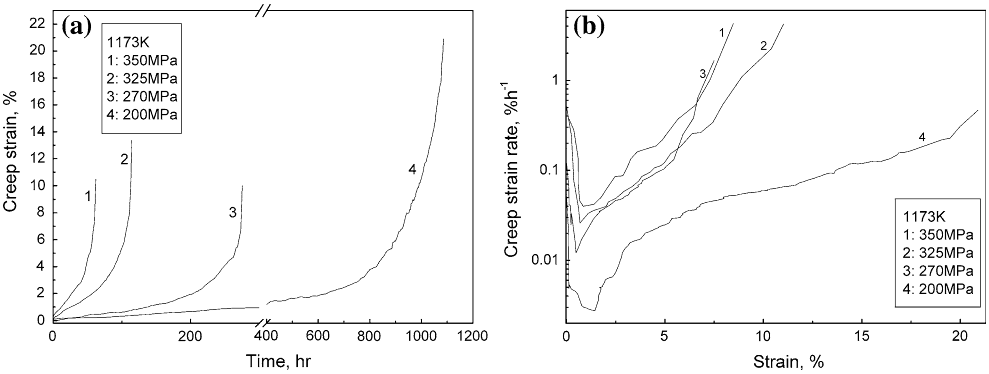

Fig. 3 Creep curves of the alloy at 1173 K: (a) strain versus time; (b) strain rate versus strain

vacancy diffusion through the lattice at very high temperature and along the grain boundaries at high temperature from dilated to compressed zones in single grains. The creep rate of diffusion creep is proportional to the applied stress and decreases when grain size increases. Bilde-Sørenson (Ref 19) explains why the *n* value deviates from 1 in diffusional creep. Boundaries with a dense coincidence-site lattice (CSL) are not effective sources and sinks of vacancies. A boundary that is close to a CSL may require a finite excess concentration of vacancies before it will absorb them (Ref 20, 21). The closer the orientation of boundary is to that of CSL, the higher this excess is. When the applied stress increases, more boundaries become effective and the *n* value deviates from 1. In common, the high values of $n = 10.4$–12 are considered to associate with shear mechanism, while the values of $n = 3.8$–4.3 are associated with dislocation climb (Ref 14-16). The two activation energies, reported frequently in multi-phase superalloys, are associated with creep controlled by dislocation motion. It has been reported (Ref 22) that the self-diffusion activation energy for Ni-based superalloys is in the range of 257–283 kJ/mol. The observed activation energy of 285 kJ/mol for the alloy at low temperature regions is very close to that of self-diffusion controlled climb mechanism, similar to that of other observations for precipitation hardened superalloys (Ref 16, 23). To understand the interaction of dislocation and γ' precipitation clearly, the microstructures of the alloy interrupted during creep are investigated.

3.3 Transmission Electron Microscopy

3.3.1 Creep at 1123 K and 425 MPa. Figure 6 is a TEM image showing the typical dislocation structure observed after 27 h (about one-third of the creep life) at 1123 K and 425 MPa, which is just at steady state stage. Although detailed Burger's vector analysis has not been undertaken, compared with the literatures (for example, those of Pollock and Argon (Ref 24), Mukherji et al. (Ref 25), and Leverant and Kear (Ref 26)), it is indicated that groups of partial dislocations may create a variety of fault configurations in γ' precipitates, and the stacking faults are generated when dislocation of type $a/3\ \langle 112\rangle$ shear the γ' particles. One established mechanism for superlattice intrinsic stacking fault (SISF) shearing (Condat and Decamps [Ref 27] and Mukherji et al. [Ref 25]) is considered here. Generally, dense dislocation networks induced by creep are mainly constrained at the γ/γ' interface. Since the SISF is lying on a common $\{111\}$ glide plane, the matrix $a/2\langle 110\rangle$ dislocations must, as totals, dissociate into partials at the γ /γ' interface, producing a single super Shockley partial gliding in the γ' particle and an $a/6\langle 112\rangle$ partial remains at the interface, which relaxes the high coherency stresses at γ/γ' interfaces. Kear and Oblak (Ref 28) and Sass et al. (Ref 29) also proposed a dislocation model for the formation of stacking faults in γ'. In this model, two similar $a/2\langle 110\rangle$ dislocations interact at the γ/ γ' interface to form an $a/2\langle 112\rangle$ dislocation that dissociates to form $a/3\langle 112\rangle$ and $a/6\langle 112\rangle$ partials. Furthermore, both partials have the parallel Burgers vectors; however, in Condat's model their Burgers vectors form an angle of 60°. According to Mukherji's investigation, the experimentally observed faults are commonly created according to Condat's model when the total creep strain is small.

After creep test of 45 h, observation of the microstructure of the alloy indicates significantly high densities of stacking faults in γ' precipitates and higher dislocation density exists in the matrix, as shown in Fig. 7. After 78 h (about two-thirds of creep life) interrupt, besides stacking faults, anti-phase boundary (APB) coupled dislocation pairs is also another precipitate shear mechanism. As has been described by Link and Feller-Kniepmeier (Ref 30), when the dominant mechanism of γ'shearing is through generation of SISF, occasionally, the paired dislocations of the type $a/2\langle 110\rangle$ are expected to get constricted upon entering the γ' cubes and the APB would be created between them, as shown in Fig. 8. In this case, pileups of matrix dislocations at the interface generate local stresses and cause a transition from SF to APB mechanism.

3.3.2 Creep at 1173 K and 350 MPa. The creep test at this condition led to a rupture time of 62 h. Sigmoidal creep does not occur and the primary creep is very short. After 25 h interrupt, the TEM image (Fig. 9) shows that the precipitates are relatively free of dislocations, and the shearing is done mainly by the APB mechanism. Dislocations, which are

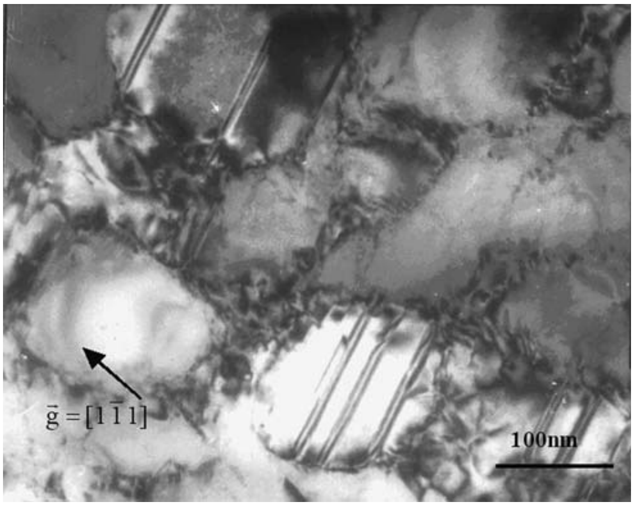

Fig. 6 TEM image showing the typical dislocation structure observed after 27 h (about one third of creep life) at 1123 K and 425 MPa

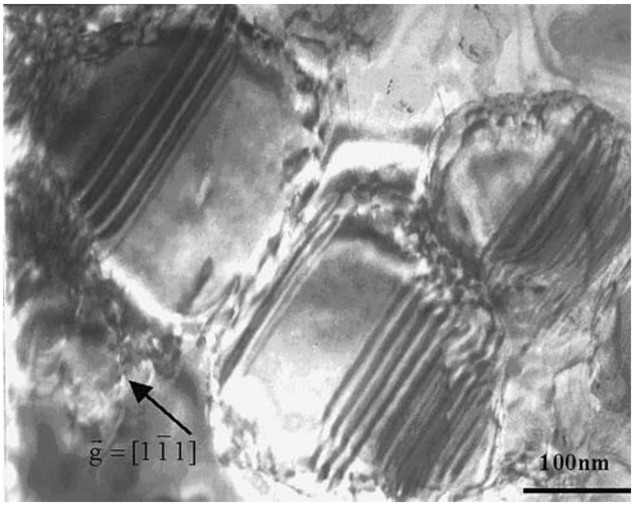

Fig. 7 TEM image showing the dislocation structure observed after creep test of 45 h at 1123 K and 425 MPa. There is an increase in precipitate shearing

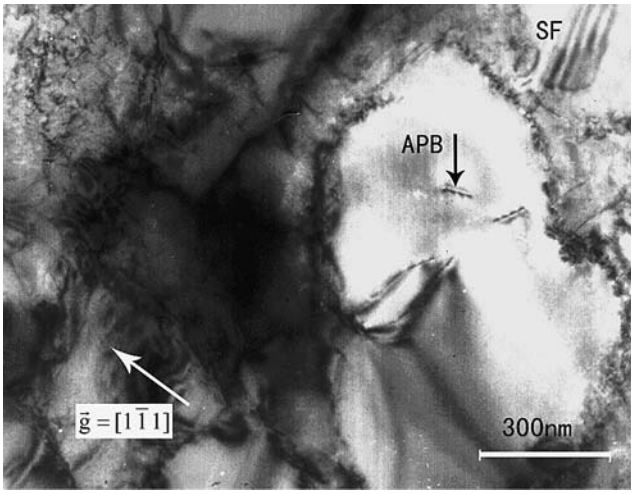

Fig. 8 TEM image showing the dislocation structure observed after 78 hours (about two thirds of creep life) at 1123 K and 425 MPa. It shows particle shearing including both APB and SF formation

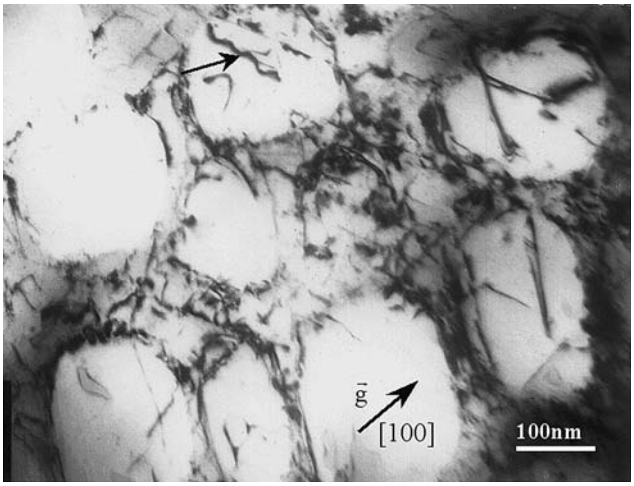

Fig. 9 TEM image after creep test of 25 h at 1173 K and 350 MPa showing the precipitates shearing involved mainly by the APB mechanism

dominantly associated with the precipitate interface, are visible over the horizontal and vertical matrix channels. Similar to the observations of Glerter and Hornbogen in a Ni–Cr–Al alloy (Ref 31), in large γ′ particles, some anti-phase boundary (APB) coupled dislocation pairs present particular morphology. As the arrow shown in Fig. 9, one of the APB dislocation pair is almost semicircular and another is almost straight, so the APB dislocation pair seems to be a zigzag curve. Nabarro and de Villiers (Ref 2) also described the mechanism of this phenomenon. When a closely coupled pair of dislocations passes through a dilute dispersion of coherent ordered larger particles, the leading dislocation is almost semicircular and the trailing dislocation is almost straight whether the dislocation pair is loosely or tightly bound. Moreover, both dislocations in the dislocation pair are almost straight, as Fig. 8 shows.

3.3.3 Creep at 1173 K and 200 MPa. Under these conditions, the dislocations are unable to cut through or bow between the particles. There is enough time for climbing and gliding and then arranging of dislocations at γ /γ′ interfaces and dislocation network formation. After 380 h interrupt test (creep life is about 1080 h), the steady-state creep is well established and the typical TEM image of the alloy is showed in Fig. 10. It is shown that dislocations migrate mainly within γ matrix in creep process and some arc-like dislocations adhere to the surface of γ′ particles, which are considered slipping from the interfaces between γ matrix and γ′ particles because their shape is the same as that of the dislocations in the interfaces. Figure 11 shows a TEM image of dislocation substructure under test conditions of 1173 K and 200 MPa for failure specimen. Very rare dislocations are observed within γ′ particles, so it is thought that particle shearing cannot operate at this condition. Furthermore, low-density dislocation within

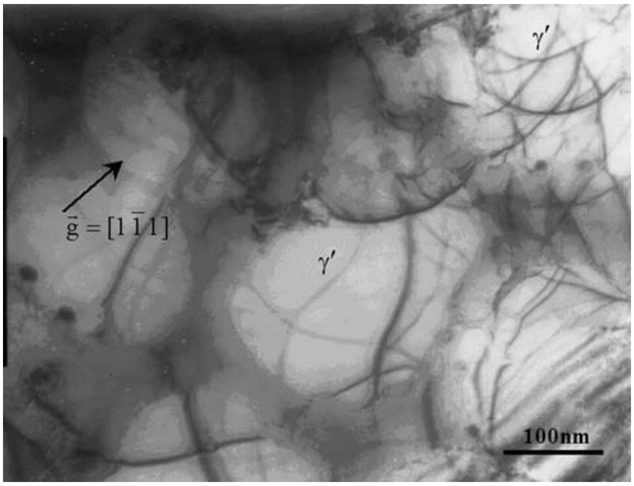

Fig. 10 TEM image after creep test of 380 hours at 1173 K and 200 MPa showing dislocation climb mechanism

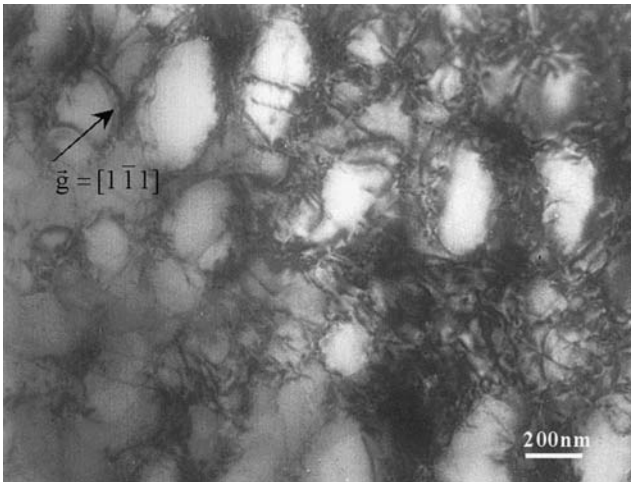

Fig. 11 TEM image of the failed specimen at 1173 K and 200 MPa showing high-density dislocation tangles at the γ/γ′ interfaces

matrix and high-density dislocation tangles at the γ/γ' interfaces is observed in this figure. It is thought that the dislocations exist at γ/γ' interfaces after climbing over γ' particles.

3.4 Deformation Mechanism Map

The creep deformation mechanisms have been confirmed by creep data analysis and microstructural investigation. At high stresses, n~14, dislocations cut through γ' particles with stacking fault (SF) and anti-phase boundary (APB) formation. At lower stresses, n~3.8 is associated with dislocation climb, and at the lowest stresses, $n < 2$, diffusional creep is the dominant mechanism. Based on these test data, the deformation mechanism map is constructed, as shown in Fig. 12. The coordinates σ/μ and T/T_m, where μ is the shear modulus and T_m is the melting temperature (= 1573 K for the alloy), are used to facilitate comparisons between different materials. Contours of constant strain rate are drawn on the map, so that the dominant creep mechanism for a given combination of stress and temperature, as well as the rate of strain predicted for this mechanism, may be read directly from the map (Ref 5, 32). The high temperature deformation mechanism map indicates a high-stress plasticity region controlled by dislocation glide, two power law creep regions and a grain boundary diffusion creep region. In practice, lattice creep mechanism would be the predominant mechanism when the stress is low and the temperature is very close to the melting point. At temperature more below the melting point and low stresses, coble or boundary creep is the dominant mechanism.

3.5 Dislocation-Creep Transitions

In this section, the dislocation-creep mechanism transitions in different stress range will be discussed based on threshold stress concept and particle hardening theories. The minimum creep rate data measured in this work do not lay on straight lines in the double logarithmic $\dot{\varepsilon}_s$ versus σ_c graph (shown in Fig. 4) excluding the possibility to simply adopt the Norton stress dependence. For dislocation creep, depending on the applied stress, the value of n changes between 3.8 and 12.1. To normalize the n values, the following relation, that includes stress and temperature dependent internal stress σ_i (σ, T), has been adopted commonly

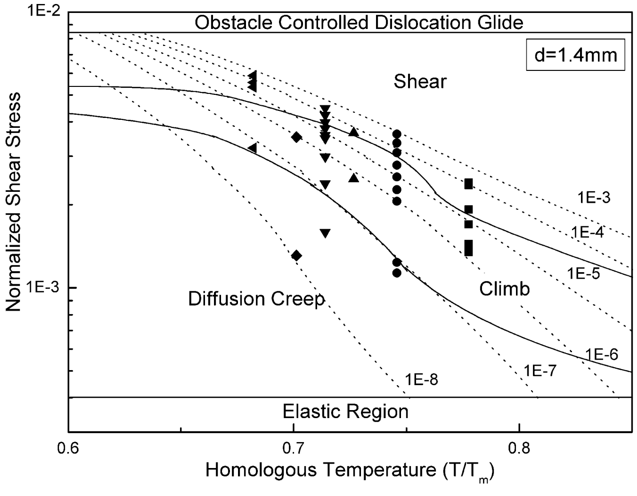

Fig. 12 A creep deformation mechanism map for the experimental alloy with an average grain size of 1.4 mm. The melting temperature T_m is 1573 K

$$\dot{\varepsilon}_s = B(\sigma_c - \sigma_i^n \exp(-Q/RT) \qquad \text{(Eq 2)}$$

where B is a material constant, and Q is the activation energy. In this way the creep rate data for a wide variety of alloys can be described with n close to a certain value (commonly 4) and values of the activation energy close to that for lattice self-diffusion.

In nickel-based superalloys, the γ' particles form obstacles to mobile dislocations. They may be sheared by single or pairs of dislocations which create stacking faults or APBs in γ' particles, or they may be circumvented by the Orowan process, which leaves a loop of dislocation surrounding each particle. Furthermore, dislocation may climb over γ' particles where a part or all of the matrix dislocation segments can extend normal to the glide plane by diffusion process. In modern superalloys, many TEM studies show that particle shearing rather than Orowan process is the dominant creep deformation mechanism at high stress levels (Ref 5–10). This can be understood through the calculation of threshold stresses for both mechanisms.

In particle hardening models, various formulae have been proposed to evaluate the critical resolved shear stress (CRSS), and those given below have been gained wide acceptance (Ref 6)

$$\text{Particle shearing: } \tau'_{PS} = \frac{\gamma_{APB}}{2b}\left[\left(\frac{4f}{\pi}\right)^{1/2} - f\right] \qquad \text{(Eq 3)}$$

$$\text{Orowan looping: } \tau_{OL} = \frac{0.4\mu b}{\pi\lambda} \cdot \frac{1}{\sqrt{1-\nu}} \ln\left(\frac{2r_s}{b}\right) \qquad \text{(Eq 4)}$$

where γ_{APB} is the anti-phase boundary (APB) energy of the particles, b the Burgers vector of matrix dislocations, f the particle volume fraction, μ the matrix shear modulus, v the Poisson ratio, λ the planar inter-particle spacing of the particles in the glide plane, and $\lambda = [(\pi/f)^{1/2} - 2\,)\cdot r_s$, r_s the average radius of the particles. The above models are developed on the basis that the second phases are widely spaced point-like obstacles. However, in nickel-based superalloys with high particle volume fraction (40–70%), the particle shearing model is not suitable, thus, Labusch and Schwarz (Ref 33) gives the modified formula

$$\tau_{PS} = 0.95(1 + C\eta_0)\tau'_{PS} \qquad \text{(Eq 5)}$$

with $\eta_0 \approx 1$ and $C \geq 1$. For overaged large size particles, the minimum value of η_0 is

$$\eta_0^{\min} = \sqrt{\frac{f}{\pi}} \qquad \text{(Eq 6)}$$

which is constant for given f, independent of the particle diameter. The Schwarz–Labusch model has been applied in some superalloys (Ref 33–35).

When particle shearing or Orowan bowing process cannot occur, it has been suggested that the dislocation is forced to surmount the particle by climb. Various models of the climb process proposed in the literatures can be broadly classified into three categories: local climb, general climb and cooperative climb (Ref 4, 8). According to geometry analysis, Mukherji and Wahi (Ref 11) point out that cooperative is a likely high temperature deformation mechanism in an alloy with high γ' volume fraction (about 70%) but is unlikely to occur in an alloy with medium γ' volume fraction (about 40% such as

IN738). In the experimental alloy, the γ' volume fraction could slightly change around 52% during creep exposure and the cooperative mechanism is also not observed (Fig. 10, 11). Considering the other climb mechanisms, Brown and Ham (Ref 6) proposed local climb model and Schewfelt and Brown (Ref 36) suggested general climb model

$$\sigma_{\mathrm{LC}} = \sigma_{\mathrm{OL}}/\sqrt{2} \qquad \text{(Eq 7)}$$

$$\sigma_{\mathrm{GC}} = \frac{f^{3/2}}{2.38}\sigma_{\mathrm{OL}} \qquad \text{(Eq 8)}$$

where σ_{LC} and σ_{GC} are dislocation resistance of local climb and general climb respectively, and σ_{OL} is the threshold stress associated with Orowan bowing.

It is seen from formula (3), the CRSS for particle shearing is dependent on γ' volume fraction. According to formula (4), the CRSS for Orowan looping depends on the size and spacing of γ' particles. These parameters could change during creep tests. In calculation, the following values of parameters have been assumed: the value of γ_{APB} varies from 0.08 J/m^2 to 0.17 J/m^2 for nickel-based superalloys in different superalloys (Ref 5-10), and an average value $\gamma_{\mathrm{APB}} = 0.12$ J/m^2 is appropriate. The value of μ measured at 1173 K is 56 GPa. The measured average effective radius of experimental alloy $r_s = 220$ nm. Burgers vector of matrix dislocations $b = 0.254$ nm. The value of v at 1173 K is 0.38. The calculated τ_{OL} is 170 MPa, τ'_{PS} is 69 MPa. It is obvious that the CRSS for particle shearing is much lower than that of Orowan looping. Thus, it is suggested that particle shearing is more favorable deformation mechanism during creep at high stresses.

According to above-mentioned models, the threshold stresses for various creep deformation mechanisms are calculated and listed in Table 2. The value of C is approximated the lower limit of $C = 1$. The threshold stress σ is transformed from τ with $\sigma \cong 2\tau$. Table 2 shows that the threshold stress for Orowan looping is much higher than that for particle shearing although it is modified by Labusch–Schwarz theory. Thus, particle shearing is easier to be observed than Orowan bowing when the applied stress is high enough. The calculated threshold stress of local climb mechanism is much higher than that of general climb. Moreover, it is higher than that of particle shearing even. From the calculated results, it can be suggested that the creep deformation is dominated by particle shearing mechanism in high stress region, while general climb is easy to happen in low stress region.

4. Conclusions

(1) The creep curves of the alloy in the temperature/stress range of 1073–1223 K/140–520 MPa were studied. The values of exponent n are calculated through variation of the steady state creep rate with stress and temperature. In high stress regions and in the temperature range of 1073–1223 K, $n = 10.4-12.1$, while in the lower stress regions and in the temperature range of 1123–1223 K, $n = 3.8-4.3$, and at the lowest stress regions, the values of n are close to 1.

(2) Different interactions between dislocations and γ' precipitates in the experimental superalloy have been observed. At high stresses, a shear mechanism involving stacking fault and/or anti-phase boundary coupled dislocation pair formation in γ' occurs. At lower stresses, dislocation climb over γ' precipitates and at the lowest stresses, diffusional creep is the dominant mechanism. Based on the creep tests at various stresses and temperatures, a deformation mechanism map is constructed, which can be used to predict the creep mechanism under a given condition.

(3) The conventional particle strengthening theories and dislocation creep theories are applied to calculate the threshold stresses of various creep deformation mechanisms, which indicates that particle shearing is easier to operate than Orowan looping at high stresses, and general climb is easy to happen at low stresses.

Table 2 Calculated threshold stresses (MPa) for creep deformation mechanisms at 1173 K

Particle shearing	Orowan looping	Local climb	General climb
184	340	241	54

References

1. J.X. Zhang, T. Murakumo, H. Harada, Y. Koizumi, and T. Kobayashi, Creep Deformation Mechanisms in Some Modern Single–Crystal Superalloys, *Superalloys*, K.A. Green, T.M. Pollock, H. Harada, T.E. Howson, R.C. Reed, J.J. Schirra, and S. Walston, Ed., TMS, Warrendale, PA, 2004, p 189–195
2. F.R.N. Nabarro and H.L. Villiers, Introduction to Creep-resistant Alloys, *Physics of Creep*, Taylor & Francis Ltd., London, 1995, p 1–14
3. R.C. Reed, N. Matan, D.C. Cox, M.A. Rist, and C.M.F. Rae, Creep of CMSX-4 Superalloy Single Crystals: Effects of Rafting at High Temperature, *Acta Mater.*, 1999, **47,** p 3367–3381
4. R.F. Decker and C.T. Sims, The Metallurgy of Nickel-Base Alloy, *The Superalloys*, C.T. Sims and W.C. Hagel, Ed., John Wiley & Sons Inc., 1972, p 33–77
5. S.A. Sajjadi and S. Nategh, A High Temperature Deformation Mechanism Map for the High Performance Ni-based Superalloy GTD-111, *Mater. Sci. Eng. A*, 2001, **307,** p 158–164
6. L.M. Brown and R.K. Ham, Dislocation-Particle Interaction, *Strengthening Methods in Crystals*, A. Kelly, and R.B. Nicholson, Ed., Elsevier, Amsterdam, 1971, p 9–12
7. F. Garofalo, Modes of Deformation in Creep, *Fundamentals of Creep and Creep-Rupture in Metals*, The Macmillan Co., New York, 1965, p 136–145
8. W.I. Mitchel, Age Hardening of High Temperature Nickel Base Alloys, *Z. Metallk.*, 1966, **57,** p 586 (In German)
9. T.C. Chou and Y.T. Chou, High-temperature Ordered Inter-metallic Alloys, *Materials Research Society Symposia Proceedings*, Vol. 39, C.C. Koch, C.T. Lin, and N.S. Stoloff, Ed., MRS, Pittsburgh, PA, 1985, p 461
10. D. Mukherji, F. Jiao, W. Chen, and R.P. Wahi, Stacking Fault Formation in γ' Phase During Monotonic Deformation of IN738LC at Elevated Temperatures, *Acta Metal Mater.*, 1991, **39,** p 515–1524
11. D. Mukherji and R.P. Wahi, Some Implications of the Particle and Climb Geometry on the Climb Resistance in Nickel-based Superalloys, *Acta Metal Mater.*, 1996, **44,** p 529–1539
12. R. Röseler and E. Arzt, The Kinetics of Dislocation Climb over Hard Particles—II. Effects of an Attractive Particle-Dislocation Interaction, *Acta Metall.*, 1988, **36,** p 1053–1060
13. J.T. Guo, C. Yuan, H.C. Yang, V. Lupinc, and M. Maldini, Creep-Rupture Behavior of a Directionally Solidified Nickel-based Superalloy, *Metall. Mater. Trans. A*, 2001, **2A**, p 1103–1110
14. K.R. Williams and B. Wilshire, On the Stress- and Temperature-dependence of Creep of Nimonic 80 A, *Met. Sci.*, 1973, **7,** p 176
15. J.P. Dennision, P.D. Holmes, and B. Wilshire, The Creep and Fracture Behaviour of the Cast Nickel-based Superalloy IN 100, *Mater. Sci. Eng.*, 1978, **33,** p 35–47

16. V. Lupinc, Creep: Introduction and Phenomenology, *Creep and Fatigue in High Temperature Alloys*, J. Bressers, Ed., Applied Science Publishers Ltd., England, 1982, p 7
17. O.D. Sherby, O.A. Ruano, and J. Wadsworth, Deformation Mechanisms in Crystalline Solids and Newtonian Viscous Behavior, *Creep Behaviour of Advanced Materials for 21st Century*, R.S. Mishra, A.K. Mukherjee, and K. Linga Murty, Ed., TMS, Warrendale, PA, 1999, p 397
18. B. Wilshire, Case Studies in Diffusional Creep, *Creep Behaviour of Advanced Materials for 21st Century*, R.S. Mishra, A.K. Mukherjee, and K. Linga Murty, Ed., TMS, Warrendale, PA, 1999, p 451
19. J. Bilde-Søensen and P.A. Thorsen, The Role of Interfacial Structure in Diffusional Creep, *Boundaries and Interfaces in Materials*, R.C. Pond, W.A.T. Clark, A.H. King, and D.B. Williams, Ed., TMS, Warrendale, PA, 1998, p 179
20. M.F. Ashby, On Interface-Reaction Control of Nabarro–Herring Creep and Sintering, *Scripta Metall.*, 1969, **3,** p 837
21. H. Gleeither, Grain Boundaries as Point Defect Sources or Sinks—Diffusional Creep, *Acta Metall.*, 1979, **27,** p 187
22. J.A. Daleo and J.R. Wilon, "GTD111 Alloy Material Study", Presented at The International Gas Turbine and Aeroengine Congress and Exhibition, Birmingham, UK, 1996
23. Z. Yang, Y. Xiao, and C. Shih, High Temperature Creep of Ni–Cr–Co Alloys and the Effect of Stacking Fault Energy, *Z. Metallkde.*, 1987, **78,** p 339–343
24. T.M. Pollock and A.S. Argon, Creep Rresistance of CMSX-3 Nickel Base Superalloy Single Crystals, *Acta Metall Mater.*, 1992, **40,** p 1–30
25. D. Mukherji, H. Gabrisch, W. Chen, H.J. Fecht, and R.P. Wahi, Mechanical Behaviour and Microstructural Evolution in the Single Crystal Superalloy SC16, *Acta Mater.*, 1997, **45,** p 3143
26. G.R. Leverant and B.H. Kear, Creep of Precipitation-Hardened Nickel-based Alloy Single Crystals at High Temperatures, *Metall. Trans.*, 1973, **4,** p 355–362
27. M. Condat and B. Decamps, Shearing of γ' Precipitates by Single a/2 110-line Matrix Dislocations in a $\gamma\gamma'$ Ni-based Superalloy, *Scripta Metall.*, 1987, **21,** p 607
28. B.H. Kear and J.M. Oblak, Deformation Modes in γ' Precipitation Hardened Nickel-based Alloys, *J Phys.*, 1974, **7,** p 35–45
29. V. Sass, U. Glatzel, and M. Feller-Kniepmerier, Anisotropic Creep Properties of the Nickel-based superalloy CMSX-4, *Acta Mater.*, 1996, **44,** p 1967–1977
30. T. Link and M. Feller-Kniepmerier, Shear Mechanisms of the γ' Phase of Single-crystal Superalloys and their Relation to Creep, *Met. Trans.*, 1992, **23A,** p 99–105
31. H. Gleiter and E. Hornbogen, Theorie der Wechselwirkung von Versetzungen mit kohärenten geordneten Zonen (II), *Phys. Stat. Sol.*, 1965, **12,** p 251 (In German)
32. H.J. Frost and M.F. Ashby, Deformation Mechanisms and Deformation-Mechanism Maps, *Deformation Mechanism Maps*, Pergamon Press, Elmsford, NY, 1982, p 3–20
33. R. Labusch and R.B. Schwarz, Dynamic Simulation of Solution Hardening, *J. Appl. Phys.*, 1978, **49,** p 5174–5187
34. W. Huther and B. Reppich, Interaction of Dislocations with Coherent, Stree-Free Ordered Particles, *Z. Metallk.*, 1978, **69,** p 628–634
35. B. Reppich, P. Schepp, and G. Wehner, Some New aspects Concerning Particle Hardening Mechanisms in γ' Precipitating Nickel-based alloys—II Experiments, *Acta Metall.*, 1982, **30,** p 95–104
36. R.S.W. Shewfelt and L.M. Brown, High-temperature Strength of Dispersion Hardened Single Crystals, *Phil. Mag.*, 1977, **35,** p 945–962